

Computational Electrochemistry: Finite Element Simulation of a Disk Electrode with Ultrasonic Acoustic Streaming

Iain E. Henley,[†] Adrian C. Fisher,^{*,‡} Richard G. Compton,[‡] and Craig E. Banks[‡]

Department of Chemical Engineering, University of Cambridge, New Museums Site, Pembroke Street, Cambridge, CB2 3RA U.K., and Physical and Theoretical Chemistry Laboratory, University of Oxford, South Parks Rd, Oxford, OX1 3QZ, U.K.

Received: September 9, 2004; In Final Form: December 20, 2004

Computer simulations using the finite element method (FEM) are used to predict the correlation between the transport limiting current (I_{lim}) and parameters such as diffusion coefficient, source to electrode separation, source power, and medium viscosity for a sonicated disk electrode in “face on” mode. The fluid dynamics and diffusion layer are modeled directly using FEM and predict that the electrode is uniformly accessible, I_{lim} is proportional to the diffusion coefficient to the $2/3$ power and I_{lim} is proportional to the square root of the source power. Curves are also calculated relating I_{lim} to the source to electrode separation and liquid viscosity.

1. Introduction

A significant amount of interest in the combination of ultrasound and electrochemistry has emerged in recent years in which the unusual physical effects produced by the propagation of ultrasound in a liquid are employed to significantly alter and improve the characteristics of electrochemical devices. Applications include the maintenance of the activity of electrode surfaces in otherwise highly passivating media (such as biological samples) via constant removal of the passivating layer,^{1,2} increased mass transport rates,³ increases in the reaction rate constants at the solid–liquid interface,⁴ and the formation of emulsions of immiscible liquids.⁵ These improvements to the traditional electrochemical methods such as anodic stripping voltammetry and linear sweep voltammetry provide a route to highly sensitive and robust analytical techniques which are extremely cost-effective compared to other analytical methods such as inductively coupled plasma–mass spectroscopy (ICP–MS) and atomic absorption spectroscopy (AAS). The principal effects that produce the observed enhancements include acoustic streaming, turbulent convection, microstreaming from oscillating bubbles, and cavitation. The effects from cavitations and acoustic streaming can produce extraordinarily large rates of convection that can significantly reduce the thickness of the diffusion layer, increase limiting currents (I_{lim}) and confer on macroelectrodes the short time scale properties of microelectrodes in voltammetric measurements. While the effects of microjets formed near the solid electrode surface by the collapse of bubbles and the motion of bubble near the electrode both aid mass transport,⁶ it is thought that acoustic streaming is the major factor influencing the convection of material to the electrode.^{7,8} The streaming is brought about by absorption of momentum by the liquid developing into a net flow in the direction of the applied sound field.

A device called a “sonotrode”⁹ utilizes acoustic streaming by attaching an electrode directly to the end of an ultrasound source. This is in general use and is robust enough to

electrochemically probe regions otherwise inaccessible by conventional hydrodynamic electrodes such as the rotating disk or channel electrode. The constant electrode cleaning effect also provides a considerably safer alternative to the dropping mercury electrode.

An alternative arrangement is to place the electrode in a “face on” mode in which the source (a focused or planar, horn transducer) is positioned opposite the electrode. A planar source generally produces a turbulent flow of liquid which, although empirical correlations have been obtained between I_{lim} and the source to electrode separation/applied power, is difficult to characterize analytically. In contrast, a focused source produces a well-defined laminar flow that can reach transport rates of 10–100 cm/s. In these conditions, and at suitably low scan rates the cyclic voltammogram (CV) is transformed to a steady state form. At ultrasound powers below a certain threshold cavitation can be minimized, removing the spikes in the voltammogram that occur above the current due to acoustic streaming. Recent analytical advances combined with numerical simulation have predicted the axial and radial streaming velocities from a focused Gaussian source.¹⁰ Stefan et al.¹¹ have correlated the velocities predicted by simulation with experimentally measured limiting currents to determine an empirical relationship between the axial velocity and I_{lim} . This work however did not simulate the diffusion layer above the electrode–liquid interface and so was limited in the scope to which direct predictions of I_{lim} against source power, electrode to source separation etc. could be made. Presented here is an extension to this work providing a full numerical characterization of the fluid velocities and the diffusion layer using FEM. These simulations are focused on “far field” type geometries at low powers to assess the effects of induced convection with complication from local turbulence etc, which may also contribute to enhancements at higher powers. Correlations are predicated for the limiting current against the source to electrode separation, the source power, the diffusion coefficient and the liquid viscosity.

2. Theory

When ultrasound is propagated in a fluid a bulk movement is induced due to the forces exerted by the sound waves. The

* Corresponding author. E-mail: adrian_fisher@cheng.cam.ac.uk.

[†] University of Cambridge.

[‡] University of Oxford.

velocity of the liquid increases with sound pressure and in a tube the resultant recirculatory flow has been shown to be time-independent after an initial build up period.¹⁰ This acoustic streaming is described by the continuity equation and the Navier–Stokes equations for an incompressible, Newtonian fluid. The driving forces are given by the momentum transfer from the sound to the fluid and are spatially distributed in the beam. In this study the equations were cast into axisymmetric form to save on computational resource (eqs 1–3).

$$\frac{1}{r} \frac{\partial}{\partial r}(ru) + \frac{\partial w}{\partial z} = 0 \quad (1)$$

$$\frac{\partial u}{\partial t} + u \frac{\partial u}{\partial r} + w \frac{\partial u}{\partial z} = F_r - \frac{1}{\rho_0} \frac{\partial p}{\partial r} + v \left(\frac{\partial}{\partial r} \left(\frac{1}{r} \frac{\partial}{\partial r}(ru) \right) + \frac{\partial^2 u}{\partial z^2} \right) \quad (2)$$

$$\frac{\partial w}{\partial t} + u \frac{\partial w}{\partial r} + w \frac{\partial w}{\partial z} = F_z - \frac{1}{\rho_0} \frac{\partial p}{\partial z} + v \left(\frac{1}{r} \frac{\partial}{\partial r} \left(r \frac{\partial w}{\partial r} \right) + \frac{\partial^2 w}{\partial z^2} \right) \quad (3)$$

where u and w are the fluid velocities in the radial (r) and axial (z) directions respectively, F_r and F_z are the forces per unit mass acting on the fluid in each axis, p is pressure, ρ_0 is the fluid density, and v is the kinematic viscosity.

For a focused ultrasound beam with a Gaussian amplitude distribution over a circular transducer (horn), the force terms are given by eqs 4–6 as derived by Kamakura et al. in reference.¹⁰

$$F_z(r,z) = \frac{\alpha}{(\rho_0 c_0)^2} |\tilde{p}|^2 \quad (4)$$

$$F_r(r,z) = \frac{2\alpha r}{(\rho_0 c_0)^2 k a^2} \frac{z/R_a - G(1 - z/d)}{(1 - z/d)^2 + (z/R_a)^2} |\tilde{p}|^2 \quad (5)$$

where the pressure amplitude is given by

$$|\tilde{p}|^2 = p_0^2 \frac{1}{(1 - z/d)^2 + (z/R_a)^2} \times \exp \left[-2 \left(\frac{r}{a} \right)^2 \frac{1}{(1 - z/d)^2 + (z/R_a)^2} \right] \quad (6)$$

and the value of α is given by

$$\alpha = \frac{(\zeta + 4\eta/3)(2\pi f)^2}{2\rho_0 c_0^3} \quad (7)$$

in which c_0 is the speed of sound in the fluid, $k = 2\pi f/c_0$, f is the sound frequency, a is the source radius, R_a is the Rayleigh distance defined as $ka^2/2$, G is the focusing gain defined as R_a/d , d is the focal length, ζ is the bulk viscosity, and η is the shear viscosity. This analytical result assumes that the wavelength is much shorter than a and that d is several times larger than a .

In our model the ultrasound source was placed opposite and in line with a disk electrode placed smoothly in the end wall of the tube as shown in Figure 1. Assuming the end wall is an ideal sound absorber for nonreflection, the governing equations were solved using the finite element method (FEM) that has been successfully employed for the study of fluid dynamics and hydrodynamic electrodes in the past.^{12–14} The model domain consisted of a rectangular region in which edges 1, 2, and 3 represented the walls of the tube at which the velocity would vanish and edge 4 was the axis of the tube.

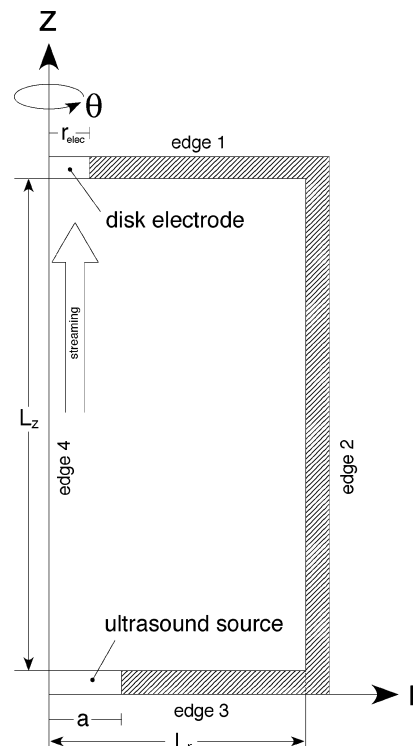


Figure 1. Tubular FEM domain modeled in cylindrical coordinates.

The integration domain was divided into a number of triangular elements, each containing six nodes¹⁶ and as in other studies the standard Galerkin residual finite element method was applied using an in-house code. The flow velocities u and w were approximated over the area of each element by the summation over six nodes of the nodal values multiplied by quadratic interpolation functions.

$$u(r,z) \approx \sum_{i=1}^6 N_i(r,z) u_i \quad (8)$$

$$w(r,z) \approx \sum_{i=1}^6 N_i(r,z) w_i \quad (9)$$

where N_i is the quadratic interpolation function of the i th node and u_i and w_i are the nodal values of the primitive variables. The pressure was similarly approximated using the three corner nodes of each element, in accordance with the practice of using a lower order interpolation for the pressure than for velocity.¹⁷

$$p(r,z) \approx \sum_{i=1}^3 M_i(r,z) p_i \quad (10)$$

where M_i is the linear interpolation function from the i th corner node.

The Galerkin residual technique was applied to the governing equations, simplified using Greens theorem and integrated using Gauss–Legendre quadrature to produce a global matrix equation that could be solved via a frontal scheme.¹⁷ The time dependence was solved via an explicit, centered time, finite difference formulation as discussed in the literature and which has been successfully used for hydrodynamic modulation in the past^{18,19}(eqs 10–12).

$$([K_u] + \frac{2}{\partial t}[K_T])\tilde{u}_1 + [K_{Pr}]\tilde{p}_1 = (-[K_u] + \frac{2}{\partial t}[K_T])\tilde{u}_0 - [K_{Pr}]\tilde{p}_0 - [K_F](F_{r1} + F_{r0}) \quad (11)$$

$$([K_w] + \frac{2}{\partial t}[K_T])\tilde{w}_1 + [K_{Pz}]\tilde{p}_1 = (-[K_w] + \frac{2}{\partial t}[K_T])\tilde{w}_0 - [K_{Pz}]\tilde{p}_0 - [K_F](F_{z1} + F_{z0}) \quad (12)$$

$$[K_{ConU}]\tilde{u}_1 + [K_{ConW}]\tilde{w}_1 = -[K_{ConU}]\tilde{u}_0 - [K_{ConW}]\tilde{w}_0 \quad (13)$$

where u_0 , w_0 , F_{z0} , F_{r0} , and p_0 are the known values of u , w , F_z , F_r , and p at time $t = 0$ or previous time steps for $t > 0$ and u_1 , w_1 , F_{z1} , F_{r1} , and p_1 are the values at the next time step. In this situation the forces do not change with time so that $F_{z0} = F_{z1}$ and $F_{r0} = F_{r1}$. The element matrices were calculated from eqs 14–17.

$$[K_u]_{ij} = \int_{A^{(e)}} v \left(r \frac{\partial N_i}{\partial r} \frac{\partial N_j}{\partial r} + \frac{1}{r} N_i N_j + r \frac{\partial N_i}{\partial z} \frac{\partial N_j}{\partial z} \right) + \left(r N_i u \frac{\partial N_j}{\partial r} + r N_i w \frac{\partial N_j}{\partial z} \right) dA \quad (14)$$

$$[K_w]_{ij} = \int_{A^{(e)}} v \left(r \frac{\partial N_i}{\partial r} \frac{\partial N_j}{\partial r} + r \frac{\partial N_i}{\partial z} \frac{\partial N_j}{\partial z} \right) + \left(r N_i u \frac{\partial N_j}{\partial r} + r N_i w \frac{\partial N_j}{\partial z} \right) dA$$

$$[K_{Pr}]_{ij} = \frac{1}{\rho_0} \int_{A^{(e)}} r N_i \frac{\partial M_j}{\partial r} dA \quad [K_{Pz}]_{ij} = \frac{1}{\rho_0} \int_{A^{(e)}} r N_i \frac{\partial M_j}{\partial z} dA \quad (15)$$

$$[K_{ConU}]_{ij} = \int_{A^{(e)}} M_i N_j + r M_i \frac{\partial N_j}{\partial r} dA$$

$$[K_{ConW}]_{ij} = \int_{A^{(e)}} r M_i \frac{\partial N_j}{\partial z} dA \quad (16)$$

$$[K_T] = [K_F] = \int_{A^{(e)}} r N_i N_j dA \quad (17)$$

in which $A^{(e)}$ is the area of each element, $[K_u]$ and $[K_w]$ come from the convective and viscous momentum transfer terms in the r and z directions, $[K_{Pr}]$ and $[K_{Pz}]$ are the pressure matrices, $[K_{ConU}]$ and $[K_{ConW}]$ come from the continuity equation and $[K_T]$ and $[K_F]$ come from the time derivative and the force terms, respectively.

The nonlinear terms in the Navier–Stokes equations required the use of an iterative solution procedure. Starting with an initial guess, which in the case of a time dependent solution would be the values at the previous time step and for steady-state calculations would be the “linearized” solution, the velocities were repeatedly refined and relaxed by taking 20% of the new solution and 80% of the previous iteration values until convergence was achieved to a pre defined tolerance. Convergence was tested by summing the square of the change in each primitive variable at each node point. When the total percentage change between successive iterations fell below $1 \times 10^{-4}\%$ then convergence was achieved. At the end of each iteration the expanding mesh around the area of the beam was further refined using an adaptive grid generation strategy based on an a posteriori error indicator. The error indication took a similar form to that presented by Nann and Heinze²⁰ where the gradient of the polynomial fit between adjacent elements was compared and if the difference was above a predefined threshold then the two elements were marked for a 50% reduction in area at the next iteration. This routine was found to produce good convergence when combined with some hand coded expanding

TABLE 1: Boundary Conditions Used to Solve the Acoustic Streaming Navier–Stokes Equations

boundary	u	w	p
edge 1	$u = 0$	$w = 0$	$\partial p / \partial z = 0$
edge 2	$u = 0$	$w = 0$	$\partial p / \partial r = 0$
edge 3	$u = 0$	$w = 0$	$\partial p / \partial z = 0$
edge 4	$u = 0$	$\partial w / \partial n = 0$	$\partial p / \partial r = 0$

TABLE 2: Boundary Conditions Used to Solve the Convection–Diffusion Equation

boundary	C
edge 1, $r \leq r_{elec}$	$C = 1$
edge 1, $r > r_{elec}$	$\partial C / \partial z = 0$
edge 2	$C = 0$
edge 3	$C = 0$
edge 4	$\partial C / \partial r = 0$

regions around the areas of most interest. The value of the threshold for refinement was chosen by trial and error such that convergence was achieved without too many elements being used. The algorithm by Shewchuk^{21,22} was used to generate a high quality mesh in which only the boundary needed to be defined a priori, and all triangle areas were guaranteed a minimum interior angle of over 20°. This allowed for rapidly expanding regions where the flow field changed the most and few elements were in the less variable parts of the grid.

The boundary conditions are shown in Table 1. A second finite element simulation was employed to determine the steady-state mass transport by diffusion and convection to and from the disk electrode at which a transport limited, one electron-transfer reaction is driven given by $A + e^- \rightarrow B$. The convection–diffusion equation (eq 18) is solved using FEM.

$$D \left(\frac{\partial^2 C}{\partial r^2} + \frac{1}{r} \frac{\partial C}{\partial r} + \frac{\partial^2 C}{\partial z^2} \right) - u \frac{\partial C}{\partial r} - w \frac{\partial C}{\partial z} = 0 \quad (18)$$

where D is the diffusion coefficient of the electroactive species and C is the normalized concentration given by $C = [A]/[A]_{bulk}$ and $[A]_{bulk}$ is the bulk concentration. The upwind streamline Petrov–Galerkin (USPG) technique was used to stabilize the finite element method for high flow rate situations in which the standard Galerkin technique is known to produce oscillatory solutions.^{23,24} In this method the weighting functions (W_k) are given by eqs 18–20.

$$W_k = N_k + \frac{\alpha_{opt} l}{2} \frac{u(\partial N_k / \partial r) + w(\partial N_k / \partial z)}{\sqrt{u^2 + w^2}} \quad (19)$$

$$\alpha_{opt} = \coth(Pe) - \frac{1}{Pe} \quad (20)$$

$$Pe = \frac{l \sqrt{u^2 + w^2}}{2D} \quad (21)$$

in which α_{opt} is calculated for each element from the Peclet number (Pe), where l is the characteristic length of the element. In the case of zero convection $Pe = 0$, $\alpha_{opt} = 0$ and the formulation is identical to that of standard Galerkin.

The mesh of elements was made from 3 noded, linear, triangle elements generated using the Shewchuk code. The values of u and w were interpolated from the Navier–Stokes grid at the node positions of the convection–diffusion grid. The boundary conditions are shown in Table 2. An adaptive grid generation strategy was applied, as before, in which the mesh was repeatedly refined until the current converged to a predefined tolerance using the method presented by Nann and Heinze; the

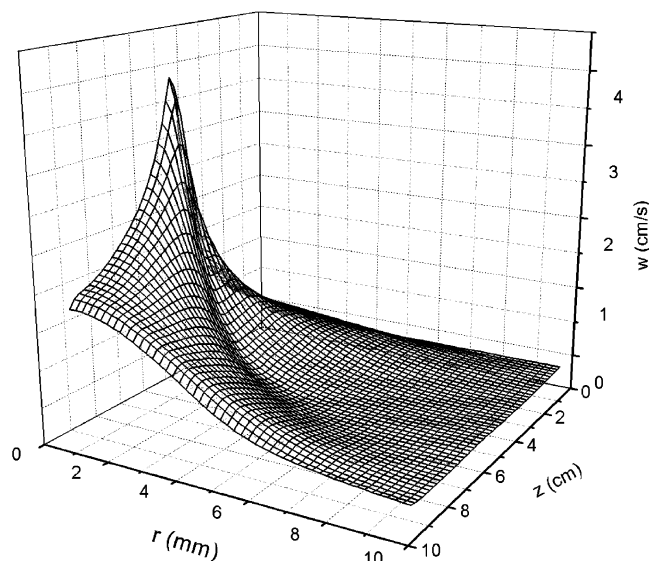


Figure 2. Axial direction streaming profile (w) built up after 5.0 s.

current was calculated by integrating the flux of C over the electrode surface (eq 22).

$$I_{\text{lim}} = n_e F D [A]_{\text{bulk}} 2\pi \int_{r_{\text{elec}}} r \frac{\partial C}{\partial z} dr \quad (22)$$

where r_{elec} is the radius of the electrode. The computer code was written in C++ and run on a Compaq Alpha XP1000 workstation.

3 Results and Discussion

3.1. Code Validation. The time-resolved buildup of streaming velocities from an initially stagnant solution was compared to previous finite difference calculations. At $t = 0$, the fluid is at rest everywhere and the ultrasound is switched on. The driving force is instantaneously generated in the beam and the fluid begins to move. The tube had dimensions $L_r = 2$ cm and $L_z = 20$ cm. The source radius (a) was 1 cm and the other conditions were: $f = 5$ MHz, $d = 5$ cm, $c_0 = 1483$ m/s, $\rho_0 = 998$ kg/m³, $\nu = 10^{-6}$ m²/s, $\zeta = 2.824 \times 10^{-3}$ kg s⁻¹ m⁻¹, $\eta = 9.98 \times 10^{-4}$ kg s⁻¹ m⁻¹, $p_0 = 60$ kPa, and $G = 21.2$. Figure 2 shows a plot of the axial velocity (w) over an r - z slice at time $t = 0.1, 0.2, 0.5, 1.0$, and 5.0 s. Once the ultrasound is switched on a peak in the axial velocity immediately begins to build up around the focal point. After a short time the nonlinear effects begin to produce the characteristic streaming of fluid which begins at the focal point and builds up along the z axis (Figure 2). Figure 3 shows the buildup of axial fluid velocity at various monitoring points along the z axis at $r = 0$. It can be seen that the velocities gradually increase and level off to a steady-state value and that the maximum velocity is observed at the focal point of the beam. These observations are in excellent agreement with the previous finite difference calculations.¹⁰ The FEM calculations predict a slightly larger velocity at the focal point, possible due to the use of a finer grid.

3.2. Steady-State Calculations. The above time dependent calculations were carried out on a fixed mesh of rectangular elements due to the difficulty involved in repeatedly adapting the grid at each time step. For steady state calculations an adaptive strategy is more convenient and allows for a high density of elements exactly where they are needed. Figure 4 shows a typical adaptively generated mesh used to solve the steady-state Navier–Stokes equations with ca. 9000 elements.

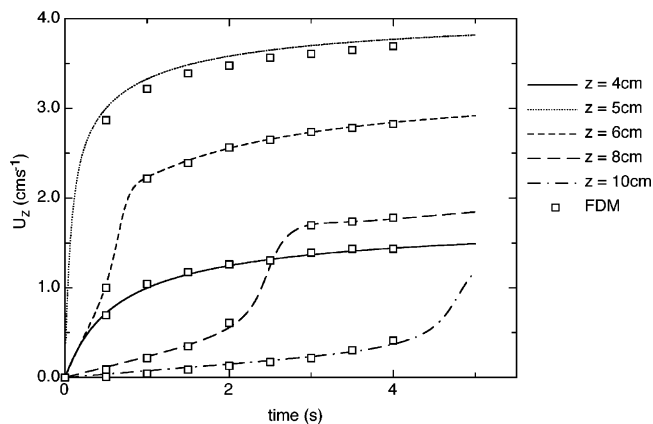


Figure 3. Axial streaming velocity at five monitoring points along the z axis for $p_0 = 60$ kPa. The lines show the FEM results and the boxes represent the FDM calculations of Kamakura et al.

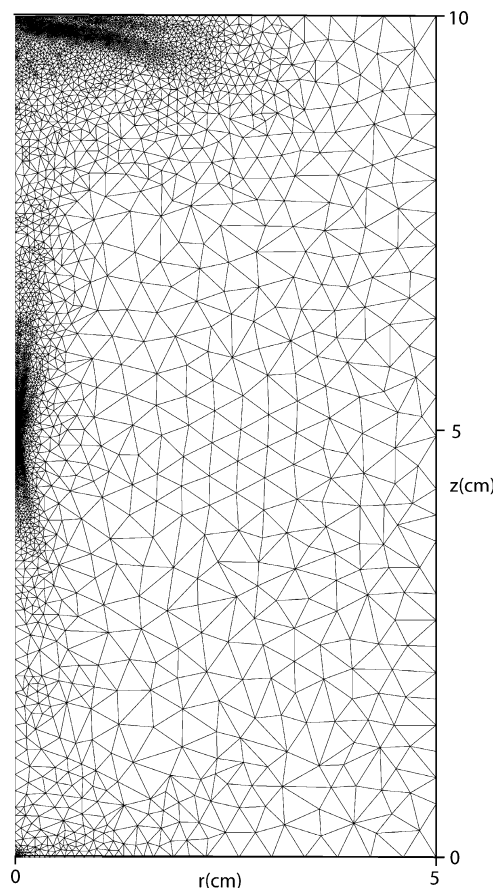


Figure 4. Adaptive finite element mesh used to solve the steady-state Navier–Stokes equations.

Most elements are concentrated around the focal point of the beam and at the point where the stream interacts with the opposite wall. This grid enables a reduction in the total FEM error.

The shape of the flow profile was investigated over the surface of the electrode to determine the hydrodynamic conditions in which the mass transport is occurring. Figure 5 shows the axial velocity (w) as a function of distance from the electrode surface for a range of radial distances (r). The cell geometry was $L_x = 5$ cm and $L_z = 10$ cm and the kinematic viscosity was 2×10^{-6} m²/s. All other parameters were as used before. The w velocity was found to have a quadratic relationship to the distance from the wall up to ~ 1.5 mm as has been demonstrated for the wall tube, hydrodynamic electrode.²⁵ The

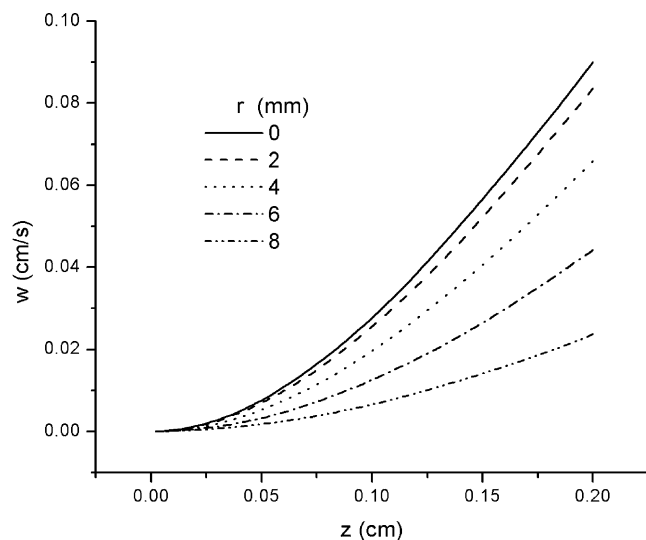


Figure 5. Axial velocity as a function of distance from electrode surface at different radial positions for $p_0 = 60$ kPa, $L_r = 5$ cm, and $L_z = 10$ cm.

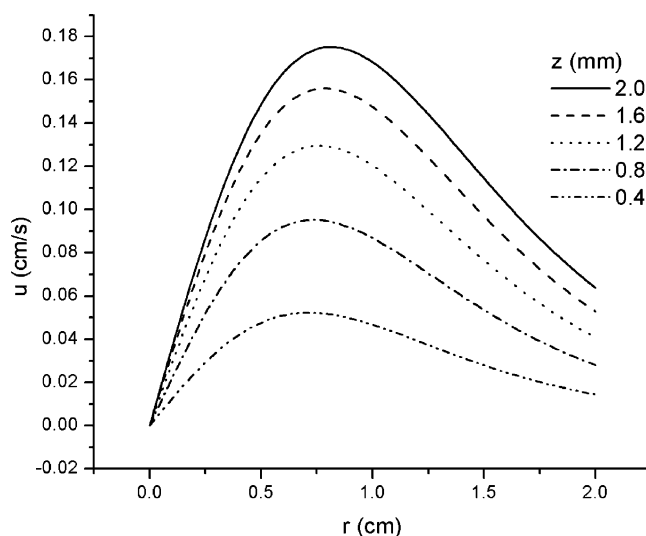


Figure 6. Radial velocity as a function of r at different axial distances above the electrode surface for $p_0 = 60$ kPa, $L_r = 5$ cm, and $L_z = 10$ cm.

radial velocity (u) is plotted in Figure 6 against r for a range of distances from the electrode in the z axis.

3.3. Current Density Distribution. The steady state limiting current on a microdisk electrode was initially simulated in the absence of forced convection and the current was found to agree with the relation²⁶ $I_{lim} = 4nFC_{bulk}Dr_{elec}$. The fluid velocities from grid in Figure 4 were then added to the simulation to solve the convection–diffusion equation. Figure 7 shows a typical adaptively refined mesh used for solving the convection–diffusion equation with the incorporation of the velocities from acoustic streaming. A close up of the region above the electrode shows that most of the refinement took place around the perimeter of the electrode.

The variation in current density along the radius of the electrode was investigated for cells of width $L_r = 5$ cm and horn to electrode separations in the range of $L_z = 10$ –18 cm. The electrode radius (r_{elec}) was 1.5 mm, the source pressure was $p_0 = 30$ kPa, viscosity was $\nu = 10^{-6}$ m²/s, and other parameters were as before. Figure 8 shows plots of the current density for each L_z value normalized to the average current density over the whole electrode. The plots show that the

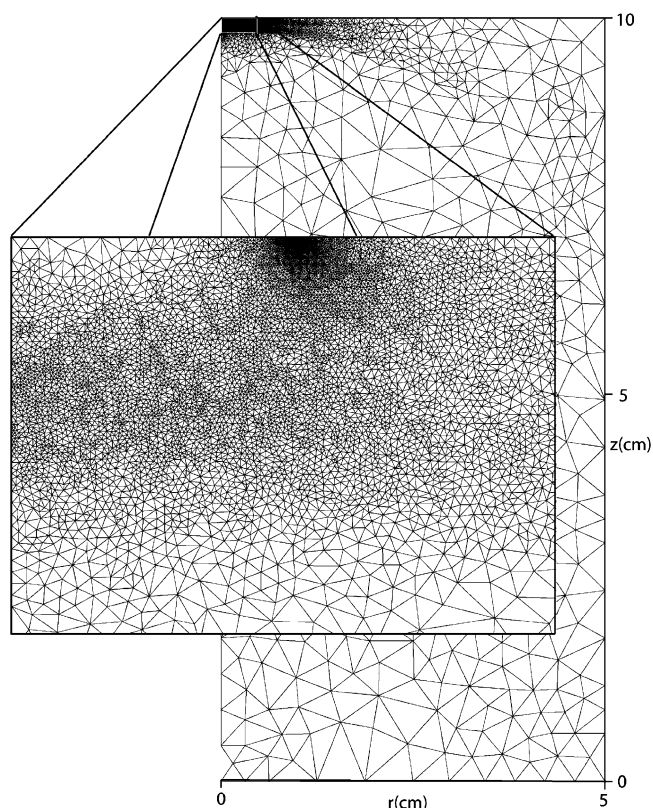


Figure 7. FEM mesh adaptively refined to solve the steady-state convection–diffusion equation.

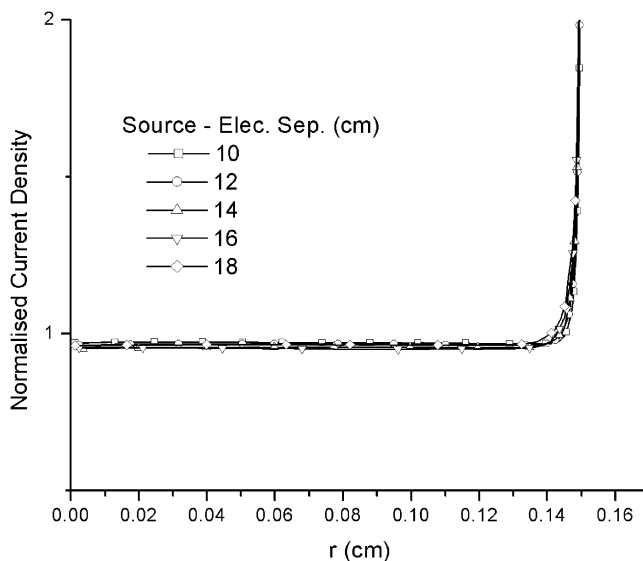


Figure 8. Current density over a 1.5 mm radius electrode at different source to electrode separations.

electrode is uniformly accessible for all these horn–electrode separations verifying work by Marken et al.^{8,27} It can also be seen that as L_z is increased a larger region at the perimeter of the electrode is effected by an “edge-effect” increase in current. This effect is quite small and can be attributed to a reduction in the radial velocity at greater distances from the horn.

3.4. I_{lim} against Diffusion Coefficient. The variation in mass transport limited current (I_{lim}) as a function of the diffusion coefficient was determined for a range of source pressures $p_0 = 10, 20, 30$, and 40 kPa. L_r was 5 cm, L_z was 10 cm, and C_{bulk} was 1 mM. Figure 9 shows that plots of I_{lim} against $D^{2/3}$ yield a straight line through zero for all source pressures used.

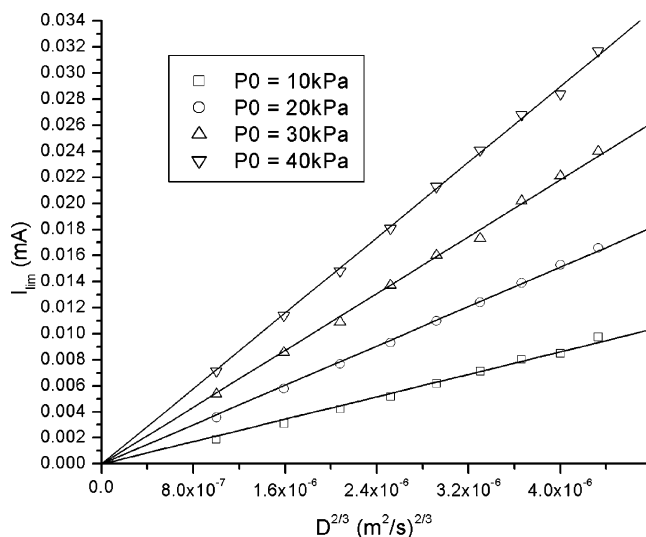


Figure 9. Variation in limiting current as a function of the diffusion coefficient for a range of p_0 values.

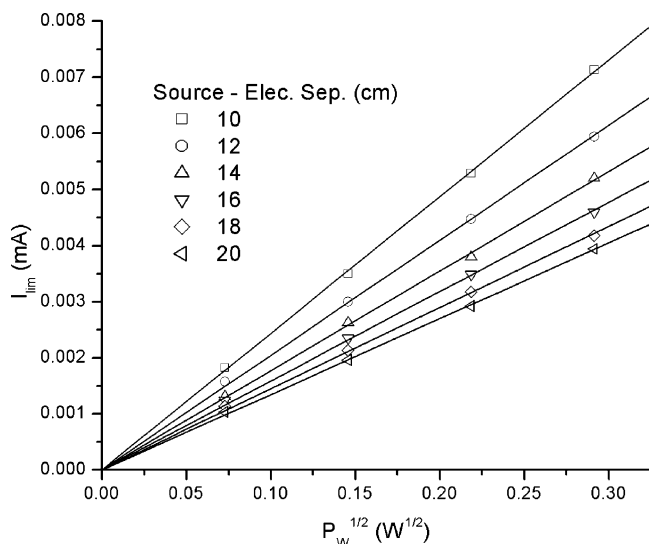


Figure 10. Variation in limiting current as a function of the acoustic radiation power for a range of source to electrode separations: $L_r = 5$ cm and $L_z = 10$ to 20 cm.

3.5. I_{lim} against Source Power. Next I_{lim} was calculated for the range of source pressures $p_0 = 10$ –40 kPa and $L_z = 10$ –20 cm. In Figure 10, I_{lim} was plotted as a function of the square root of the acoustic radiation power (P_w)^{1/2} derived from the relation.

$$P_w = \frac{\pi a^2}{4\rho_0 c_0} p_0^2 \quad (23)$$

Each plot yielded a straight line through zero for the range of L_z values investigated.

3.6. I_{lim} against Viscosity. The dependence of the limiting current on the kinematic viscosity in the range $\nu = 1 \times 10^{-6}$ to 4.5×10^{-5} m²/s was investigated for a cell of dimensions $L_r = 5$ cm by $L_z = 10$ cm and $p_0 = 30$ kPa. From eqs 4–6, it can be seen that both r and z components of the force on the liquid increase with shear viscosity while at the same time the increase in kinematic viscosity acts to reduce the streaming velocities. These two effects combine to produce the curve in Figure 11 that shows a decrease in current with viscosity. A simple power relationship fit could not be obtained for the whole curve but the closest was in the region of $I_{lim} \propto \nu^{-1/3}$.

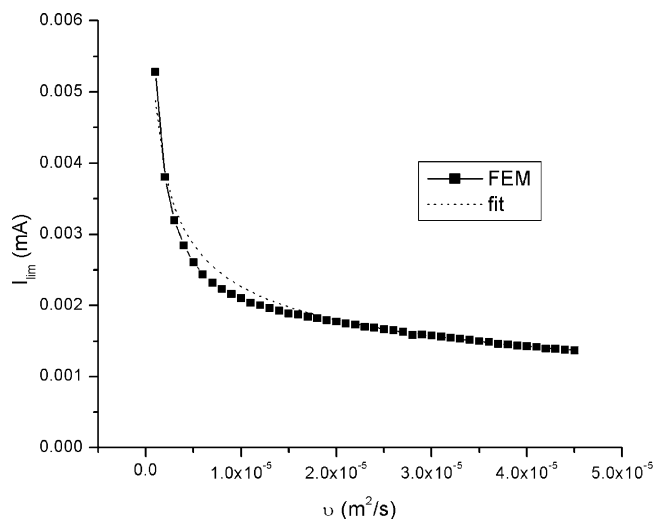


Figure 11. Plot of limiting current against kinematic viscosity with $p_0 = 30$ kPa, $L_r = 5$ cm, and $L_z = 10$ cm. A curve fit is shown of the function $5 \times 10^{-8} \nu^{-1/3}$.

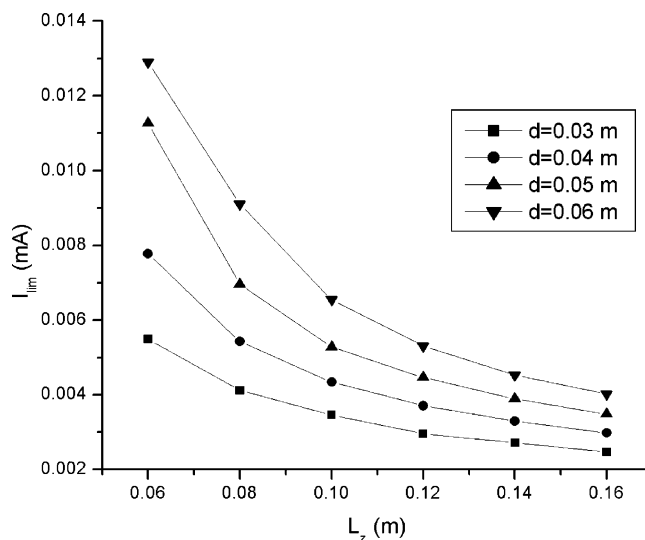


Figure 12. Plots of I_{lim} against source to electrode separation for a range of focal lengths.

3.7. I_{lim} against Source to Electrode Separation (L_z). The effect of the distance between the source and the electrode on the limiting current was investigated for $L_r = 5$ cm, $L_z = 6$ to 16 cm and for focal lengths $d = 3, 4, 5$, and 6 cm (Figure 12). In general for $L_z > d$, a decrease in current was observed for larger values of L_z due to the reduction in axial velocity as a result of spreading of the beam in the radial direction via viscous momentum transfer. By bringing the focal point nearer the electrode the limiting current could be increased substantially.

The above trends in viscosity, diffusion coefficient and source power have recently been highlighted in an experimental investigation by Compton.²⁸

4. Conclusions

Axisymmetric FEM codes have been successfully developed to solve the fluid dynamic and convection–diffusion equations governing the thinning of the diffusion layer over a disk electrode by acoustic streaming induced by an ultrasound source. The codes have been validated by comparison to previous finite difference codes with good correlation. By systematically varying the simulation parameters and geometry, empirical relationships were predicted between I_{lim} and key parameters

such as diffusion coefficient, source to electrode separation, source power, and liquid viscosity. These curves verify previous experimental results and so confirm the assumption that acoustic streaming is the principle mechanism of enhanced mass transport in sono-electrochemical cells of this design. The flow profile was found to be analogous to a wall tube electrode and the electrode was found to be uniformly accessible. The flexible nature of FEM and the mesh generation method used allow the code to be readily extended to detailed analysis of new sono-electrochemical device geometries as well as transient voltammetry.

References and Notes

- (1) Tomcik, P.; Banks, C. E.; Compton, R. G. *Electroanalysis* **2003**, *15*, 1661.
- (2) Kruusma, J.; Banks, C. E.; Neil, L.; Compton, R. G. *Anal. Chim. Acta* **2004**, *510*, 85.
- (3) Banks, C. E.; Compton, R. G. *ChemPhysChem* **2003**, *4*, 169.
- (4) Jung, C. G.; Chapelle, F.; Fontana, A. *Ultrasonics Sonochem.* **1997**, *4*, 117.
- (5) Banks, C. E.; Compton, R. G. *Electroanalysis* **2002**, *15*, 329.
- (6) Birkin, P. R.; Silva-Martinez, S. J. *Electroanal. Chem.* **1996**, *416*, 127.
- (7) Cooper, E. L.; Coury, L. A. *J. Electrochem. Soc.* **1998**, *145*.
- (8) Marken, F.; Akkermans, R. P.; Compton, R. G. *J. Electroanal. Chem.* **1996**, *415*, 55.
- (9) Compton, R. G.; Eklund, J. C.; Marken, F.; Rebbitt, T. O.; Akkermans, R. P.; Waller, D. N. *Electrochim. Acta* **1996**, *42*, 2919.
- (10) Kamakura, T.; Matsuda, K.; Kumamoto, Y. *J. Acoust. Soc. Am.* **1995**, *97*, 2740.
- (11) Stefan, I. C.; Mo, Y.; Zanelli, C. I.; Scherson, D. A. *Anal. Chem.* **2001**, *73*, 4384.
- (12) Stevens, N. P. C.; Fisher, A. C. *J. Phys. Chem. B* **1997**, *101*, 8259.
- (13) Stevens, N. P. C.; Hickey, S. J.; Fisher, A. C. *An. Quim.* **1997**, *93*, 225.
- (14) Gooch, K. A.; Williams, N. A.; Fisher, A. C. *Electrochem. Commun.* **2000**, *2*, 51.
- (15) Henley, I. E.; Fisher, A. C. *J. Phys. Chem.* **2003**, *107*, 6579.
- (16) Dhat, G.; Touzot, G. *The Finite Element Method Displayed*; Wiley-Interscience Pub.: New York, 1984.
- (17) Taylor, C.; Hughes, T. G. *Finite Element Programming of the Navier–Stokes Equations*; Pineride Press Ltd.: Swansea, U.K., 1981.
- (18) Rao, S. S. *The Finite Element Method in Engineering*; Pergamon Press: Oxford, U.K., 1982.
- (19) Gooch, K. A.; Fisher, A. C. *J. Phys. Chem. B* **2002**, *106*, 10668.
- (20) Nann, T.; Heinze, J. *Electrochem. Commun.* **1999**, *1*, 289.
- (21) Shewchuk, J. R. Engineering a 2D Quality Mesh Generator and Delaunay Triangulator. <http://www.cs.cmu.edu/~quake-papers/triangle.ps>.
- (22) Ruppert, J. *J. Algorithms* **1995**, *18*, 548.
- (23) Zienkiewicz, O. C.; Taylor, R. L. *The Finite Element Method, Fluid Dynamics*; Butterworth Heinemann: Oxford, U.K., 2000; Vol. 3.
- (24) de Sampaio, P. A. B.; Coutinho, A. L. G. A. *Comput. Methods Appl. Mech. Eng.* **2001**, *190*, 6291.
- (25) Melville, J.; Simjee, N.; Unwin, P. R.; Coles, B. A.; Compton, R. G. *J. Phys. Chem. B* **2002**, *106*, 2690.
- (26) Aoki, K.; Akimoto, K.; Tokuda, K.; Matsuda, H.; Osteryoung, J. J. *Electroanal. Chem.* **1984**, *171*, 219.
- (27) Marken, F.; Rebbitt, T. O.; Booth, J.; Compton, R. G. *Electroanalysis* **1997**, *9*, 19.
- (28) Banks, C. E.; Compton, R. G.; Fisher, A. C.; Henley, I. E. *Phys. Chem. Chem. Phys.* **2004**, *6*, 3153.